Collective Thomson scattering diagnostic with in situ calibration system for velocity space analysis in large helical device

Collective Thomson scattering diagnostic with in-situ calibration system for velocity space analysis in Large Helical Device

Masaki Nishiura,[1,2,a)] Shun Adachi,[3] Kenji Tanaka,[1,3] Shin Kubo,[4] Naoki Kenmochi,[1] Takashi Shimozuma,[1] Ryoma Yanai,[1] Teruo Saito,[5] Hideo Nuga,[1] and Ryosuke Seki[1]

[1]*National Institute for Fusion Science, 322-6 Oroshi-cho, Toki, 509-5292 Gifu, Japan*

[2]*Graduate School of Frontier Sciences, The University of Tokyo, Kashiwa, 277-8561, Japan*

[3]*Interdisciplinary Graduate School of Engineering Science, Department of Advanced Energy Engineering, Kyushu University, Kasuga, Fukuoka, 816-8580, Japan*

[4]*Chubu University, Kasugai, Gifu, 487-8501, Japan*

[5]*Research Center for Development of Far-Infrared Region, University of Fukui, Fukui, 910-8507, Japan*

[a]Author to whom correspondence should be addressed: nishiura@nifs.ac.jp

ABSTRACT

A collective Thomson scattering (CTS) diagnostic with a +/- 3 GHz band around a 77 GHz gyrotron probe beam was developed to measure the velocity distribution of bulk and fast ions in high-temperature plasmas. We propose a new in-situ calibration method for a CTS diagnostic system combined with a raytracing code. The method is applied in two situations for electron cyclotron emission (ECE) in plasmas and in a CTS diagnostic with a modulated probe beam. Experimental results highlight the importance of refraction correction in probe and receive beams. The CTS spectrum is measured with the in-situ calibrated CTS receiver, and responds to fast ions originating from a tangential neutral beam with an energy of 170 keV and from a perpendicular beam with an energy of 60 keV, both in the Large Helical Device. From a velocity space analysis model, the results elucidate the measured anisotropic CTS spectrum caused by fast ions. The calibration methods and analyses demonstrated here are essential for CTS, millimeter-wave diagnostics, and electron cyclotron heating required under fusion reactor conditions.

I. INTRODUCTION

Alpha particle confinement in a fusion reactor is an important issue in self-burning plasmas. Knowledge of the self-burning physics relevant to energetic charged particles is essential for controlling the plasmas produced. Collective Thomson scattering (CTS) is one method used for diagnosing bulk and fast ion properties in fusion plasmas, and CTS diagnostics must satisfy the collective condition $1/|\boldsymbol{k}^{\delta}|\lambda_D >> 1$. Here, λ_D is the Debye length, and the fluctuation wave number $\boldsymbol{k}^{\delta} = \boldsymbol{k}^{s} - \boldsymbol{k}^{i}$, where $\boldsymbol{k}^{i}$ and $\boldsymbol{k}^{s}$ are the incident and scattered wavenumbers, respectively. In high-temperature plasma experiments, CTS diagnostics require a modulated probe beam with megawatt-class power to extract a scattered radiation superimposed in the background radiation of electron cyclotron emission (ECE). In low-temperature and high-density plasmas, CTS is achieved using an Nd-YAG laser.

CTS diagnostics in the millimeter-wave range have been performed in the Large Helical Device (LHD) [1], TEXTOR [2], ASDEX Upgrade [3], Wendelstein 7-X [4], FTU [5], and designed for ITER [6]. CTS diagnostics share a megawatt-class gyrotron, the transmission lines and steering mirrors of an electron cyclotron heating (ECH) system. In LHD plasma experiments, measured CTS spectra have qualitatively responded to changes in ion temperature, recorded using charge exchange recombination spectroscopy (CXRS) [1]. However, the discrepancy of the ion temperature between the CTS and CXRS has quantitatively remained. We considered that the problem is caused by incorrect calibration factors relating to the CTS receiver, originating from the fact that electron temperatures of a CTS measurement, in the order of keV, are three orders of magnitude higher than those of the calibration sources used. In the experiments [1], liquid nitrogen (LN_2) at 77 K (6.63 meV) and a blackbody source at 1273 K (0.1 eV) have been used to obtain the calibration factors for the CTS receiver by extrapolating the linear outputs of the receiver to a few keV range. To solve the linearity assumption, ECE from plasmas has been used to

calibrate the CTS receiver in the practical keV range. In addition, the calibration using ECE had a merit to contain a transmission loss of mirrors and corrugated waveguides. We combined the temperature profiles obtained using YAG laser Thomson scattering (TS) for the absolute calibration, because the ECE spectra gives only the relative intensity for the receiver channels. However, the discrepancy described in the ref. [1] between the ion temperatures obtained using CTS and those obtained using CXRS remains.

In this paper, we combine the plasma experiments with a raytracing simulation, and extend the previous calibration method with ECE to use the time evolution of a plasma that increases the number of effective calibration points for the CTS receiver and performs its calibration over a wide temperature range. During a discharge, the receiver field of view is corrected using a ray trace code (TRAVIS code) [7] with the profiles of electron density and temperature measured by TS. The new in-situ method is applied to the CTS diagnostic system using on-off timing in the modulated probe beam during CTS measurement. Because the practical alignment of ECH and CTS system is difficult in a fusion reactor, the techniques we report here are applicable to the alignment method for an ECH antenna system in a fusion reactor on demand.

II. CTS DIAGNOSTIC SYSTEM AT THE LHD

The ECH system at the LHD is equipped with mega-watt class gyrotrons with frequencies of 77 GHz. These sources and their transmission lines are available for the probe and receive beams of the CTS diagnostic [1, 8, 9]. Figure 1

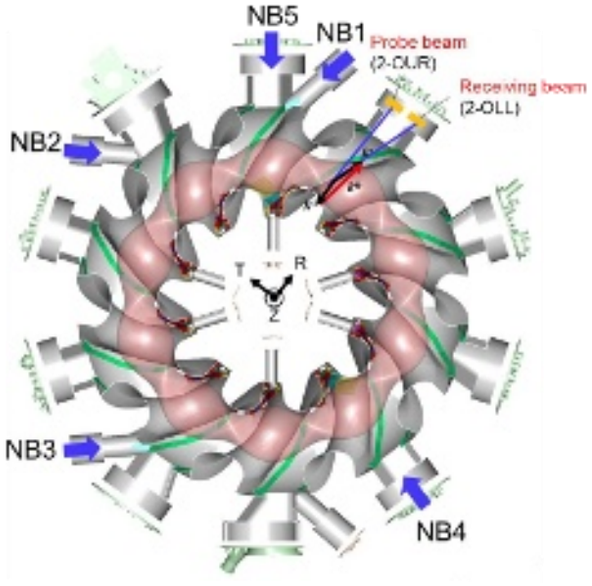

FIG. 1. Top view of LHD. The probe and the receive beams are located at the 2-OUR and 2-OLL ports, respectively. The wavevectors are scaled to understand the geometry.

shows typical geometries for the probe beam from the 2-OUR port and the receive beam from the 2-OLL port in the vacuum vessel. Steering mirrors are located near the plasma and are used to scan the beam direction to either the toroidal or the poloidal direction. A waveguide switch is located on the transmission line of the gyrotron and directs the connection either to the CTS receiver or the gyrotron.

A diagram of the CTS receiver system is shown in Fig. 2. The heterodyne receiver comprises a notch filter and a band pass filter in a radio frequency (RF) stage, a mixer, low noise amplifiers, and crystal detectors in an intermediate frequency (IF) stage. In the RF stage, the narrow-band notch filter attenuates stray radiation of gyrotron ~120 dB at a central frequency of 76.95 GHz, with a bandwidth of ±130 MHz in the RF stage. This removes any stray radiation created by the probe beam from the signal. The pass band of the band pass filter is 74 to 80 GHz. The IF, ranging from 0 to 6 GHz, is created by mixing an RF signal of 74–80 GHz with a local oscillator signal of 74 GHz. The IF signal is divided into a filter bank system and a fast digitizer system. The filter bank system has 32 channels and measures the IF signal from 0.5 to 6 GHz by the bandpass filters with passbands of 100 MHz, and 200 MHz. The diode-detector outputs of the filter bank receiver deviate from the linearity. Therefore, the input-output characteristics for all channels are required for calibration to obtain frequency spectra. are connected to video amplifiers. The outputs are input into AD converters (National Instruments PXI-6133 and PXI-6152).

The fast digitizer has a nominal bandwidth of 5 GHz and a sampling rate of 12.5 G sample/s. A fast Fourier transform reconstructs a fine feature of CTS spectrum with a narrow frequency resolution from the time-domain signal. The measurement of a radiation source with a known temperature gives each channel a calibration factor that converts the unit from voltage to electron temperature. We have previously reported that the CTS spectrum obtained using the fast digitizer system agrees well with that obtained using the filter bank system [1].

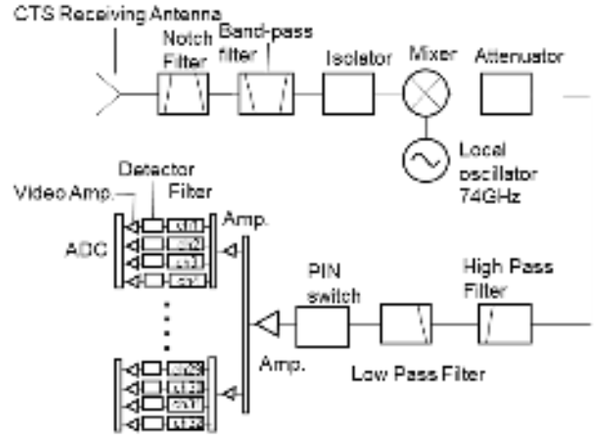

FIG. 2. Schematic diagram of the CTS receiver.

III. CALIBRATIONS OF THE CTS DIAGNOSTIC SYSTEM

A. Input and output characteristics of CTS receiver

For characterization of the CTS receiver, the signal generators SG1 (Keysight Technologies, E4431B) from 0.25 to 2 GHz and SG2 (Anritsu's MG37022A) from 2 to 6 GHz produces a test signal. They are introduced into the IF stage. The output levels for SG1 and SG2 are conditioned from -100 to -73 dBm by a variable attenuator. Figure 3 shows the characteristics of the output signals for channel 5 with a bandwidth of 200 MHz and a central frequency of 1.7 GHz (75.7 GHz in the RF stage); and for channel 16 with a bandwidth of 100 MHz and a central frequency of 2.8 GHz (76.8 GHz in the RF stage). The channels selected correspond to fast and bulk ions. The output signal increases linearly below ~1 V as the power of the test signal P_{IF} to the IF stage increases. Increasing the output level higher than ~1 V causes a deviation from the linear dependence of both channels on the outputs. Thus, the input and output characteristics for all channels determine relative calibration factors.

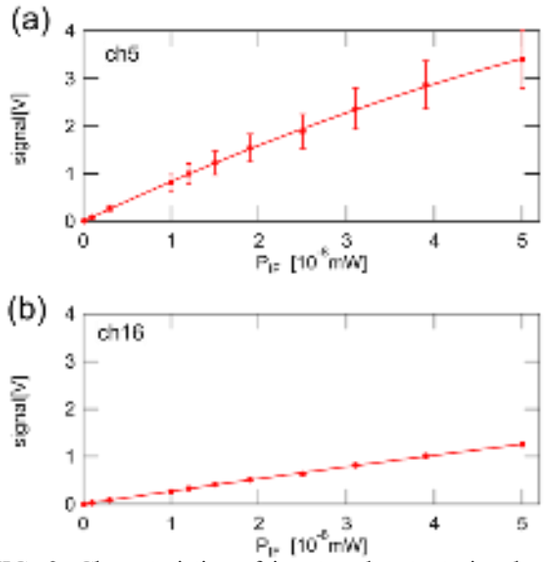

FIG. 3. Characteristics of input and output signals using signal generators. (a) channel 5 and (b) channel 16 correspond to fast and bulk ions, respectively.

B. ECE calibration source for CTS receiver

In the previous section, we characterized the relative sensitivities between the channels. ECE from LHD plasmas and the spatial profiles of electron temperature T_e and electron density n_e from the TS were combined to determine the absolute calibration factors for all channels of the CTS receiver. Because of the spatial gradient of n_e, the refraction of the receive beam with the 77 GHz band occurs at n_e of ~ 2×10^{19} m^{-3} and causes an error in the spatial position of the ECE. In addition, the frequency shift of the receive beam arises from the relativistic effect and the Doppler effect. A ray-trace code TRAVIS is used to correct these effects.

The TRAVIS code was developed for plasma-wave physics research on heating, current drive, and ECE measurement for stellarators and tokamaks in 3D magnetic equilibrium. Ray-tracing equations are solved with a weakly relativistic model. The code treats absorption, current drive, and emissivity with a fully relativistic model. The observed frequency ω is written as:

$$\omega = \frac{\omega_{ce}}{\gamma} \pm k_{||} v_{||} , \quad (1)$$

where γ is the Lorentz factor, and ω_{ce} is the local electron cyclotron frequency. $k_{||}$ and $v_{||}$ are the wave number and the electron velocity parallel to the magnetic field, respectively. The electron thermal velocity is written as:

$$v = \left(\frac{2k_B T_e}{m}\right)^{\frac{1}{2}} , \quad (2)$$

where k_B is the Boltzmann constant. If $\gamma \gg 1$, ω downshifts from ω_{ce}. In the case of observation perpendicular to the magnetic field, the central frequency of 76.8 GHz for channel 16 of the CTS receiver becomes 75.3 GHz at T_e = 10 keV due to relativistic effects.

The Doppler effect in the observed ω appears in the second term on the right hand side of Eq. (1). For an electron density higher than 10^{19} m^{-3}, the isotropization time of the electrons [10] is of the order of 100 ms. Assuming $T_{e||} = T_{\perp}$, we found that the frequency broadening for 76.8 GHz at T_e = 2 keV is about ± 2.5 GHz.

C. Receiver sensitivity calibration corrected by raytracing and absorption coefficient

The radiation transport equation describes the relation between the emission and absorption of ECE in plasmas. The radiation intensity $I(s)$ as expressed by an equivalent radiation temperature at a position s along the receiver line-of-sight becomes [11, 12] with unit [eV]:

$$\frac{dI(s)}{ds} = j(s) - \alpha(s) I(s) , \quad (3)$$

where $j(s)$ is the emissivity, $\alpha(s)$ is the absorption coefficient, and $\tau(s)$ is the optical depth. Equation (3) is integrated over the path, giving:

$$I(s) = \int_{s_0}^{s} T_e(s') \alpha(s') e^{-\tau(s')} ds' \quad (4)$$

where $T_e(s')$ is the electron temperature of the ray. By integrating $\alpha(s')$ over s' on a ray, $\tau(s)$ is expressed as:

$$\tau(s) \equiv \int_{s_0}^{s} \alpha(s')\, ds' \quad (5)$$

Here, $\tau(s)$ and $\alpha(s)$ on the ray are calculated using the TRAVIS code, which uses the TS data and outputs $T_e(s)$ and $n_e(s)$. These parameters are used to calculate $I(s)$ in Eq. (4). The calibration factors for all channels are determined

from the relation between $I(s)$ and the ECE signal measured at each time step.

Figure 4 shows the discharge waveforms for LHD#166201 for a toroidal magnetic field B_t = 2.75 T on the magnetic axis R_{ax} = 3.9 m. The ECH starts up the discharge at t = 3.0 s, following the tangential neutral beams NB2 and NB3 and the perpendicular neutral beam NB5; this sustains the plasma from t = 3.3 to 5.3 s. The steering mirror 2-OLL at (R, T, Z) = (6.8, -0.3, -0.16) directs the target to (R, T, Z) = (3.9, 0.55, 0), (see the coordinate (R, T, Z) in Fig. 1). The bottom panel in Fig. 4 shows the ECE signal for channel 5 by the assumption of a linear line-of-sight and $I(s)$ expected by the raytracing calculation. Although the ECE signal and $I(s)$ respond to the time evolution of the plasma, the refraction effect of the viewing chord mainly shifts the measured location toward the outer radial location, resulting in a decrease in I(s) compared with the linear line-of-sight throughout the discharge. When the line averaged electron density $\bar{n}_e$ of the center chord is higher than 2.0×10^{19} m^{-3}, the deviation in I(s) from the ECE signal increases. This is because refraction of the rays moves the ECE layer outwards with respect to the higher temperature location. The sudden increases in $\bar{n}_e$ at t = 3.92 and 4.52 s cause the large refraction of the viewing chord due to the pellet injections. At t = 5.3 s, the ECH and the tangential NB1 continue to sustain the plasma. The refraction of the measurement line-of-sight becomes smaller when the

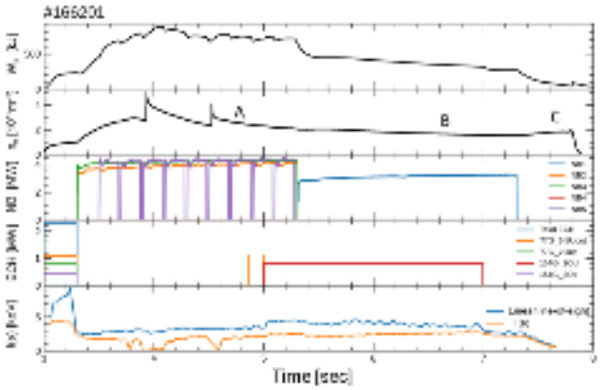

FIG. 4. Discharge waveforms for LHD shot#166201. The ECE signal, with a straight viewing chord at channel 5, and $I(s)$, calculated using the raytracing code with the TS data, are plotted in the bottom panel.

The raytracing calculation requires the time evolved electron temperature and density profiles $T_e(r/a_{99})$ and $n_e(r/a_{99})$. Those data come from the TS diagnostic and the plasma equilibrium calculation using a normalized minor radius r/a_{99}. Figure 5 shows the electron density and temperature profiles at t = 5.0 s. The 32 channels of the CTS receiver cover the core area from r/a_{99} = - 0.2 to 0.2, assuming that the rays are in a straight line. The raytracing calculation shows that the rays begin to refract at the plasma edge, even though the electron density is three or more times lower than the cutoff density for a frequency of 77 GHz. This is because the rays pass through the density gradient area due to their oblique propagation to magnetic surfaces.

Figure 6 shows the relation between the output of the CTS receiver and T_e from the ECE signal, with a linear line-of-sight and $I(s)$ at t = 4.8 s–7.8 s. The optical depth τ = 2.5–8 in this shot is chosen for a local emission measurement. When the signal moves from label A to label B, the rays are strongly affected by refraction. The input and output characteristic below the test signal of 2 mW in

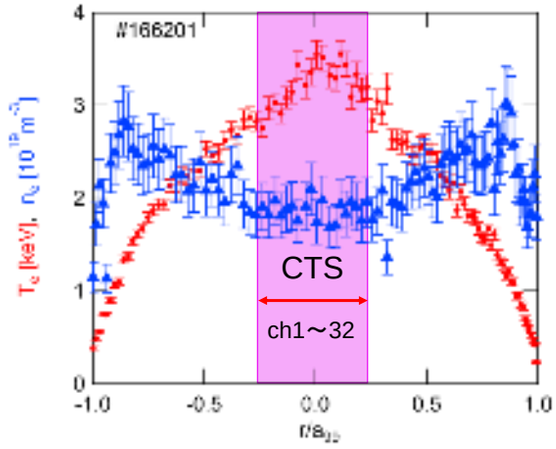

FIG. 5. Electron temperature and density profiles at t = 5.0 s for LHD shot#166201. The CTS receiver channels cover the hatched area.

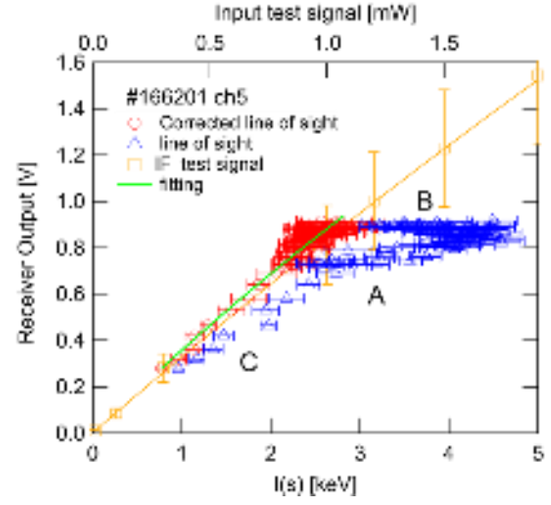

FIG. 6. ECE signal measured by channel 5 of the CTS receiver at 4.8–7.59 s. Triangles represent T_e calibrated by ECE and TS measurements before raytracing correction. Open circles correspond to I(s) after raytracing correction.

The output signal (squares) is measured when we apply the IF test signal to the receiver. The upper axis is scaled to fit the observed signals between A and C.

Fig. 3 (a) is superimposed on Fig. 6 as a reference signal. Raytracing calculation evaluates the local emission point appropriately, particularly above 0.7 V receiver output where the refraction influences the ray trajectory. The slight disagreement between I(s) and IF test signal is caused by an error of ray at the plasma edge because the TRAVIS code does not treat ray in plasmas at $r/a_{99} > 1$. To obtain the calibration curve for channel 5, $I(s)$ obtained from the raytracing calculation is fitted with a quadratic curve in Fig. 6. When the receiver output is 0.8 V, T_e is 4.5 keV in the linear line-of-sight, but $I(s)$ corrected by the raytracing calculation decreases to 2.5 keV, and the error is 2 keV.

If T_e is higher than that used here, we must consider the relativistic and Doppler effects as noted in the second term in the right hand side of Eq. (1) because of thermal broadening with respect to the viewing direction. The flat T_e profile is conducive to reducing the calibration error of the CTS receiver system.

IV. BULK AND FAST ION MEASUREMENT

A. In-situ calibration during CTS measurement

The probing beam of the CTS diagnostic is modulated with a duty cycle of 25 ms on/ 25 ms off to extract the scattered radiation from the mixture of scattered radiation and background ECE. In-situ calibration is performed using the background ECE during the off time of the gyrotron output. During CTS measurement, the advantage of this calibration method is that the CTS receiver can be calibrated in an actual measurement environment and does not require a dedicated calibration shot. Figure 7 shows the input and

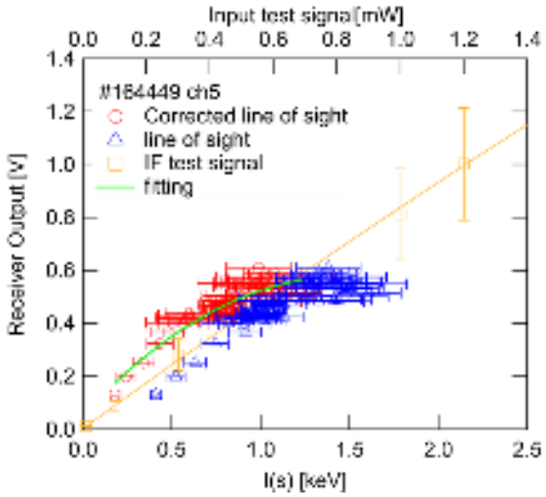

FIG. 7. ECE signal measured by channel 5 of the CTS receiver during CTS measurement. Triangles represent T_e calibrated by ECE and TS measurements. Open circles correspond to I(s) after raytracing correction. The output signal (squares) is the same as that in Fig. 6.

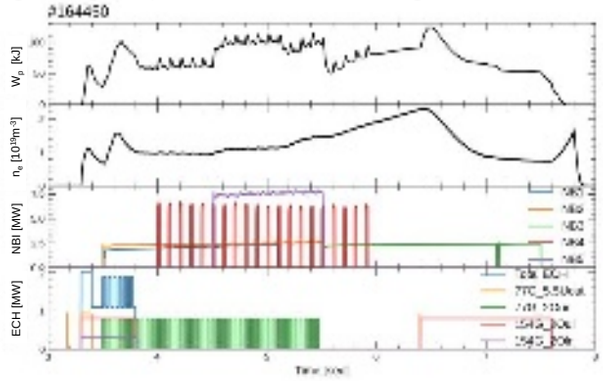

FIG. 8. Discharge waveforms for LHD shot#164450.

output characteristics of the receiver in the cases of linear line-of-sight and raytracing correction. Because the electron density is less than 2.0×10^{19} m^{-3}, the refraction of the receive beam is suppressed compared to the shot in Fig. 6. Because the effect of multi-reflection is contained when $\tau < 2.5$, $\tau = 0.6$–5 is selected by the raytracing calculation in this shot. As shown in Fig. 7, the measured data are fitted using a least-squares method to obtain the calibration curve. The appropriate degree of the polynomial used was determined using the Akaike information criterion to prevent overfitting. A quadratic equation was most appropriate for the calibration curves.

Figure 8 shows the discharge waveform with the CTS measurement for LHD shot#164450 at $R_{ax} = 3.9$ m and $B_t = 2.538$ T. A counter-NB1 and co-NB2 with an energy of 170 keV are injected to sustain the discharge. A perpendicular NB5 with an energy 64 keV is superimposed on the plasma for the additional plasma heating at $t = 4.5$–5.5 s. A perpendicular NB4 with an energy of 60 keV is modulated for CXRS measurement from $t = 4.0$ s. The bottom panel of Fig. 8 shows that the probe beam (2-OUR) is modulated with a frequency of 20 Hz at $t = 3.5$–5.5 s. The output power is 0.792 MW. The receive beam is set to a fixed direction when we measured the spatial profiles of CTS spectra. Figure 9 shows the time evolution of channel 13, dominated by bulk ion features. The scattered radiation rises and falls rapidly with the modulation of the probe beam, while the background ECE level is almost unchanged. The response of the CTS signal is different from that of the ECE signal caused by the electron heating in the ECR layer. In the case of electron heating, the transition time is much slower than that of the scattering phenomena, because it is related to the confinement time of the electrons in the plasma. The CTS signal of channel

13 begins to increase from $t = 4.5$ s when the NB5 injection begins, and further increases when the counter-NB1 injection ends at $t = 5.1$ s. The CTS signal begins to increase with co-NB2 and NB5 fast ions. This behavior indicates that the CTS diagnostic is sensitive to the ions along with the $\boldsymbol{k}^{\delta}$ direction perpendicular to the magnetic field and that the confinement of fast ions worsens by the counter fast ions. However, the reason should be analyzed in detail.

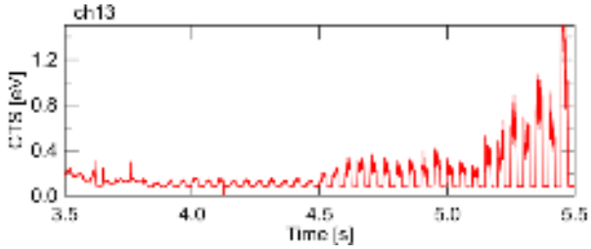

FIG. 9. Receiver signal of channel 13, containing scattered radiation and background ECE in LHD shot#164450.

B. Beam overlap and correction in CTS diagnostic

Plasma affects the trajectories of the probe and the receive beams used for CTS diagnostics. The overlap between the two beams shifts to a different location with respect to the overlap location by the straight line-of-sight. As described in Section III, the TRAVIS code is used to calculate the probe and the receive beam trajectories to determine the overlap location. The beam sizes increase in width to several tens of mm. Assuming that the beam trajectory is a straight line-of-sight, the intersections of the probe and the receive beams are $r/a_{99} = 0$, 0.26, and 0.57. In contrast, after raytracing correction, the intersections with refraction move to $r/a_{99} = 0.24$, 0.32, and 0.65. Figure 10 shows that T_i decreases by 10% and the changes in n_e and T_e are small at the core region. This result is qualitatively consistent with the fact that the ion temperature is lower than that of CXRS in reports of CTS measurement [1].

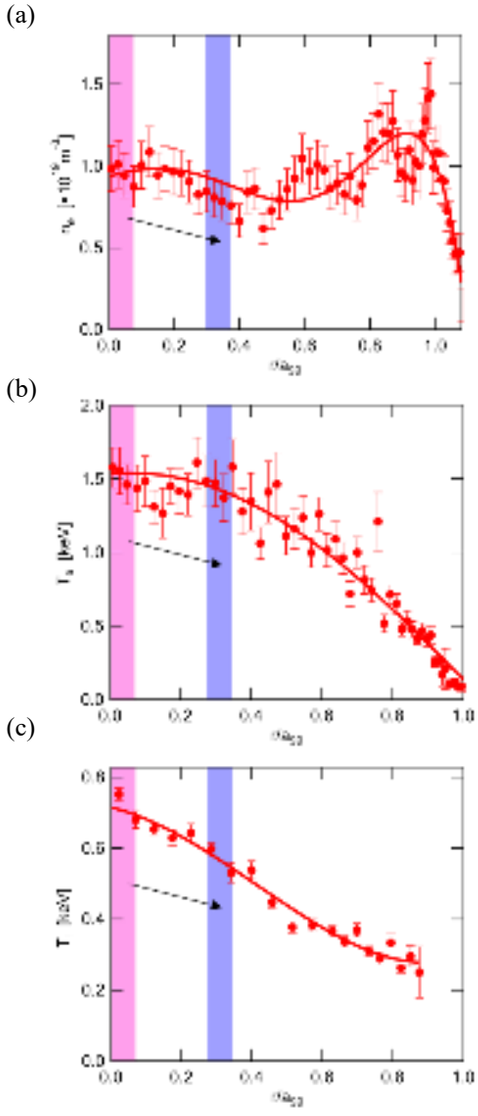

FIG. 10. (a) Electron density and (b) electron temperature from TS at $t = 5.113$ s, and (c) ion temperature from CXRS at $t = 5.1225$ s for LHD shot#164450.

C. Comparison with calculated spectrum of bulk ion temperature

For the evaluation of plasma parameters, in particular ion temperature, it is necessary to compare the measured CTS spectrum with the calculated one determined by nuisance parameters. The CTS spectra with NB5 at $t = 3.82$ and without NB5 at $t = 4.52$ s are selected in Fig. 11. The measurement position corrected by the raytracing calculation is located at $r/a_{99} = 0.32$. The CTS spectrum of bulk ions is calculated with $T_i = 0.53$ keV obtained by CXRS, and $T_e = 1.35$ keV and $n_e = 0.83\times 10^{19}$ m^{-3} obtained by TS, and is plotted in black. Because the measured T_i is 0.53 keV, the spectral broadening of bulk ion is insufficient for fitting the CTS spectrum.

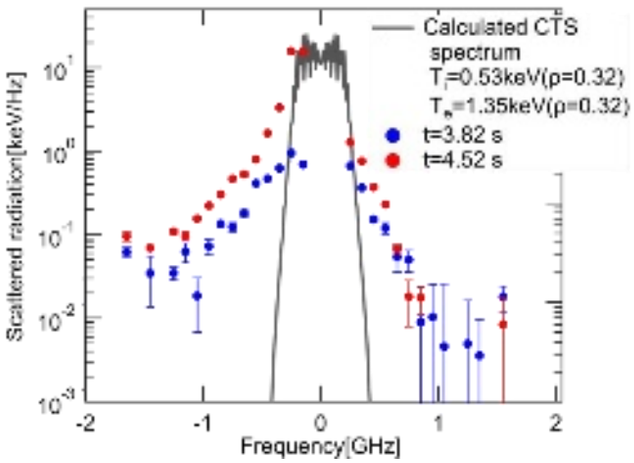

FIG. 11. CTS spectra at t = 3.82 and 4.52 s for LHD shot#164450. The theoretical CTS spectrum for bulk ions in black is calculated using data from TS and CXRS. The fast ion component is not included in the CTS spectrum. The negative and positive frequencies correspond to Co-NB2 and counter-NB1 directions, respectively.

In terms of the fast ion components of the CTS spectrum in Fig. 11, the intensity of the CTS spectrum increases strongly near the bulk ion region after NB5 injection at t = 4.52 s. The observation line-of-sight is set to the angle $\angle(\boldsymbol{k}^{\delta}, \boldsymbol{B})$ = 104.3°, which is a slight deviation from the incident pitch angle of 90° of NB5. Thus, the measured signal is sensitive to the abundant fast ions of NB5 originating in the velocity space ($v_{\parallel}$, $v_{\perp}$). In addition, asymmetry in the spectra is observed at t = 3.82 s and 4.52 s for frequencies above 0.5 GHz and below -0.5 GHz. The negative frequency coincides with the fast ion direction of co-NB2. To comprehend the spectrum asymmetry observed by the CTS diagnostic, the tomography on velocity space should be considered based on the forward modeling in the ref. [13]. The one-dimensional velocity distribution function $g(u)$ that was a projection onto $\boldsymbol{k}^{\delta}$ needed to be reconstructed into a two-dimensional velocity distribution function $f(v_{\parallel}, v_{\perp})$ on velocity space [1]. In a recent paper, we reported a velocity space reconstruction from a measured CTS spectrum using a machine learning method [9]. The $f(v_{\parallel}, v_{\perp})$, with a Gaussian distribution modeled for simplicity, provided the forward model of $g(u)$ calculated from the observation direction $\boldsymbol{k}^{\delta}$. The training data set of $f(v_{\parallel}, v_{\perp})$ and $g(u)$ trains the inversion algorithm to concatenate the relation between $g(u)$ related to a measured CTS spectrum and $f(v_{\parallel}, v_{\perp})$ we should find on velocity space. We successfully demonstrated this tomographic method for CTS diagnostics to obtain $f(v_{\parallel}, v_{\perp})$ from a $g(u)$ given. A more predictive model ensured that the sensitive frequency for co- and counter- fast ions agreed with the test function, which had Gaussian distribution, replacing the training data set produced by the TASK/FP [14] outputs in LHD plasmas. The result will be shown elsewhere. We found that the asymmetric shapes of the CTS spectrum are caused by co- and counter-anisotropic distributions in the velocity space.

V. CONCLUSION

In CTS measurement, using a 77-GHz gyrotron, we demonstrated the in-situ calibration methods of a receiver and the correction of measurement positions to enhance the accuracy in bulk and fast ion velocity space analysis.

With respect to calibration of the millimeter-wave receiver system, we pointed out the importance of considering relativistic effects, Doppler broadening, and refraction of the receiver's line-of-sight in an ECE light source. Multi-point measurement with raytracing correction is effective in producing a calibration curve for the CTS receiver. CTS diagnostics are demonstrated using in-situ calibration and measurement of ON-OFF timing, injecting a modulated probe beam. The proposed method is reliable and valuable for a reactor-relevant system.

In future work, simulation should be used for the quantitative evaluation of anisotropic fast ions. The combination of TASK/FP code and machine learning-based velocity space tomography highlights comprehension of the measured data if forward modeling is possible.

Acknowledgments

This work was supported by the JSPS KAKENHI (Grant No. 19KK0073) and NIFS budgets (NIFS21KLPR054).

Data Availability

The data that support the findings of this study are available from the corresponding authors upon reasonable request.

[1]M. Nishiura, S. Kubo, K. Tanaka, R. Seki, S. Ogasawara, T. Shimozuma, K. Okada, S. Kobayashi, T. Mutoh, K. Kawahata, T. Watari, the LHD Experiment Group, T. Saito, Y. Tatematsu, S. B. Korsholm, and M. Salewski, Nucl. Fusion 54, 023006 (2014).

[2]H. Bindslev, S. K. Nielsen, L. Porte, J. A. Hoekzema, S. B. Korsholm, F. Meo, P. K. Michelsen, S. Michelsen, J. W. Oosterbeek, E. L. Tsakadze, E. Westerhof, and P. WoskovPhys. Rev. Lett. 97, 205005(2006).

[3]S. K. Nielsen, M. Stejner, J. Rasmussen, A. S. Jacobsen, S. B. Korsholm, F. Leipold, M. Maraschek, F. Meo, P. K. Michelsen, D. Moseev, M. Salewski, M. Schubert, J. Stober, W. Suttrop, G. Tardini, D. Wagner, and the ASDEX Upgrade Team, Plasma Phys. Control. Fusion 57, 035009 (2015).

[4]D. Moseev, M. Stejner, T. Stange, I. Abramovic, H. P. Laqua, S. Marsen, N. Schneider, H. Braune, U. Hoefel, W. Kasparek, S. B. Korsholm, C. Lechte, F. Leipold, S. K. Nielsen, M. Salewski, J. Rasmussen, M. Weißgerber, and R. C. Wolf, Rev. Sci. Instrum. 90, 013503 (2019).

[5]B. Baiocchi, W. Bin, A. Bruschi, L. Figini, U. Tartari, E. Alessi, and O. D'Arcangelo, J. Instrum. 15, C01046 (2020).

[6]S. B. Korsholm, H. Bindslev, V. Furtula, F. Leipold, F. Meo, P. K. Michelsen, D. Moseev, S. K. Nielsen, M. Salewski, M. Stejner, Nucl. Instrum. Methods Phys. Res. 623, 677 (2010).

[7]N. B. Marushchenko, Y. Turkin, and H. Maassberg, Comput. Phys. Comm. 185, 165 (2014).

[8]K. Tanaka, M. Nishiura, S. Kubo, T. Shimozuma, and T. Saito, J. Instrum. 10, C12001 (2015).

[9]M. Nishiura, K. Tanaka, S. Kubo, T. Saito, N. Kenmochi, H. Nuga, R. Seki, T. Shimozuma, Y. Yoshimura, H. Igami, H. Takahashi, T. I. Tsujimura, R. Yanai, Y. Tatematsu, and the LHD Experiment Group, J. Instrum. 15, C01002 (2020).

[10]A. S. Richardson, 2019 NRL Plasma Formulary, Naval Research Laboratory, (2019).

[11]G. Bekefi, *Radiation Processes in Plasmas*, (Wiley, 1966).

[12]Hans-Jürgen Hartfuß and Thomas Geist, *Fusion plasma Diagnostics with mm-Waves*, (Wiley, 2013).

[13]M. Salewski, S. Nielsen, H. Bindslev, V. Furtula, N. Gorelenkov, S. Korsholm, F. Leipold1, F. Meo, P. K. Michelsen, D. Moseev and M. Stejner, Nucl. Fusion 51 083014 (2011).

[14]H. Nuga, R. Seki, S. Kamio, K. Ogawa, M. Isobe, M. Osakabe, M. Yokoyama, Nucl. Fusion 59, 016007 (2019).

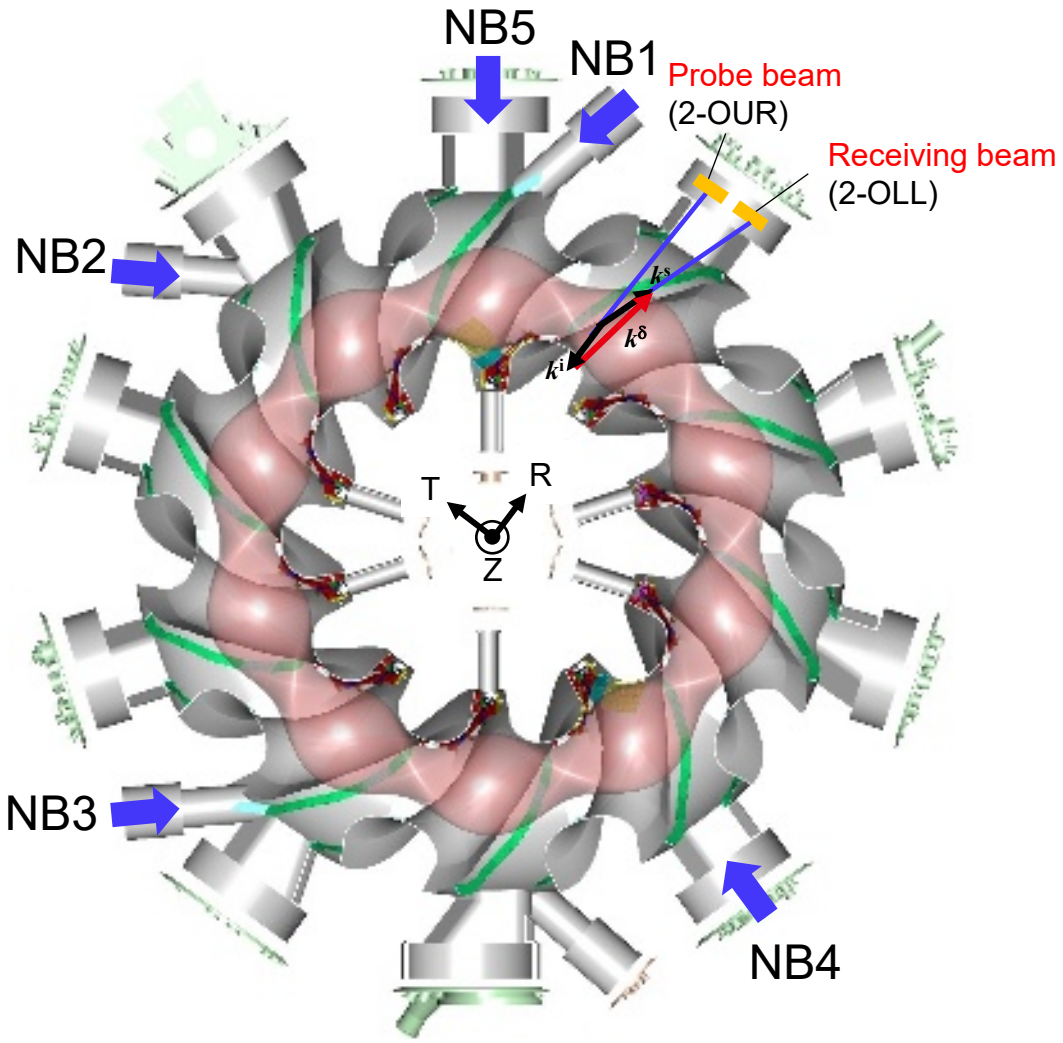
NB5
NB1
Probe beam
(2-OUR)
Receiving beam
(2-OLL)
NB2
k^s
k^δ
k^i
T
R
Z
NB3
NB4

Fig.1

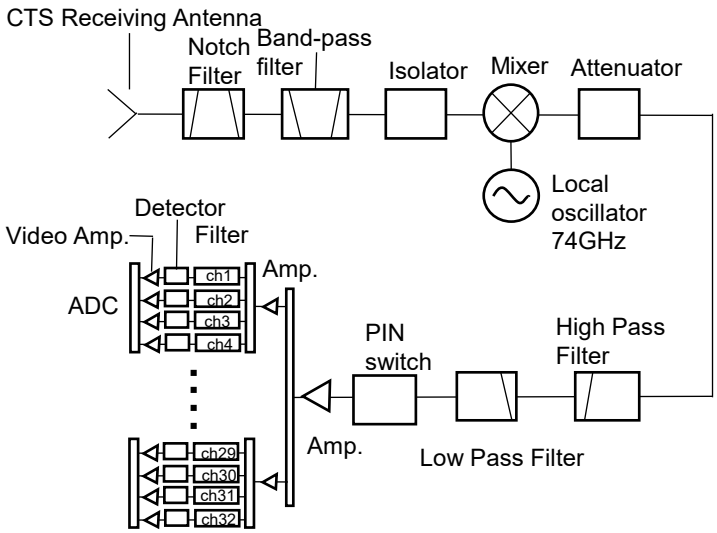
CTS Receiving Antenna
Notch Filter
Band-pass filter
Isolator
Mixer
Attenuator
Local oscillator 74GHz
Detector
Video Amp.
Filter
ADC
ch1
ch2
ch3
ch4
Amp.
PIN switch
High Pass Filter
Amp.
Low Pass Filter
ch29
ch30
ch31
ch32

Fig.2

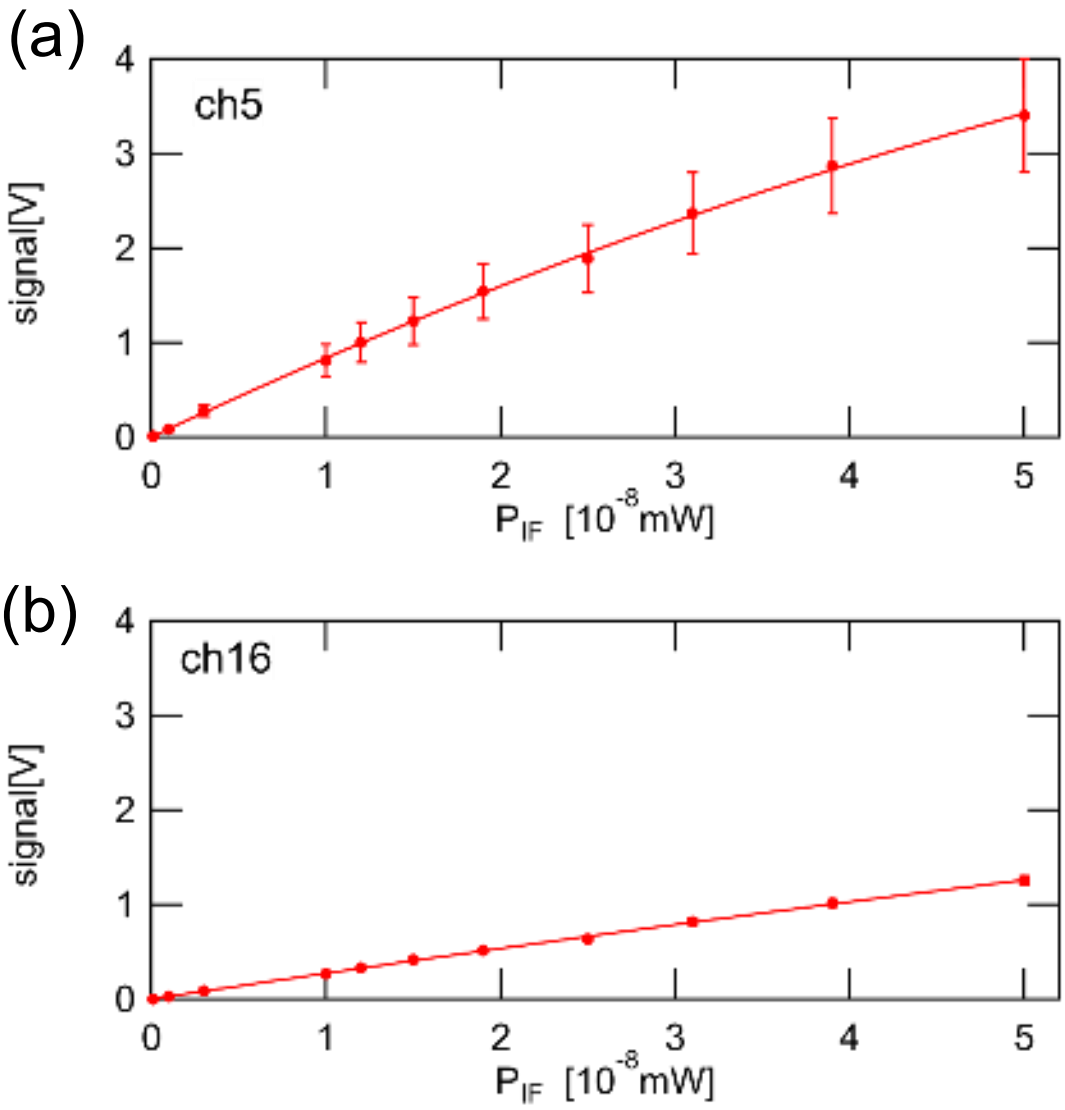
(a)
ch5
signal[V]
0
1
2
3
4
0
1
2
3
4
5
P_IF [10^-8 mW]
(b)
ch16
signal[V]
0
1
2
3
4
0
1
2
3
4
5
P_IF [10^-8 mW]

Fig.3

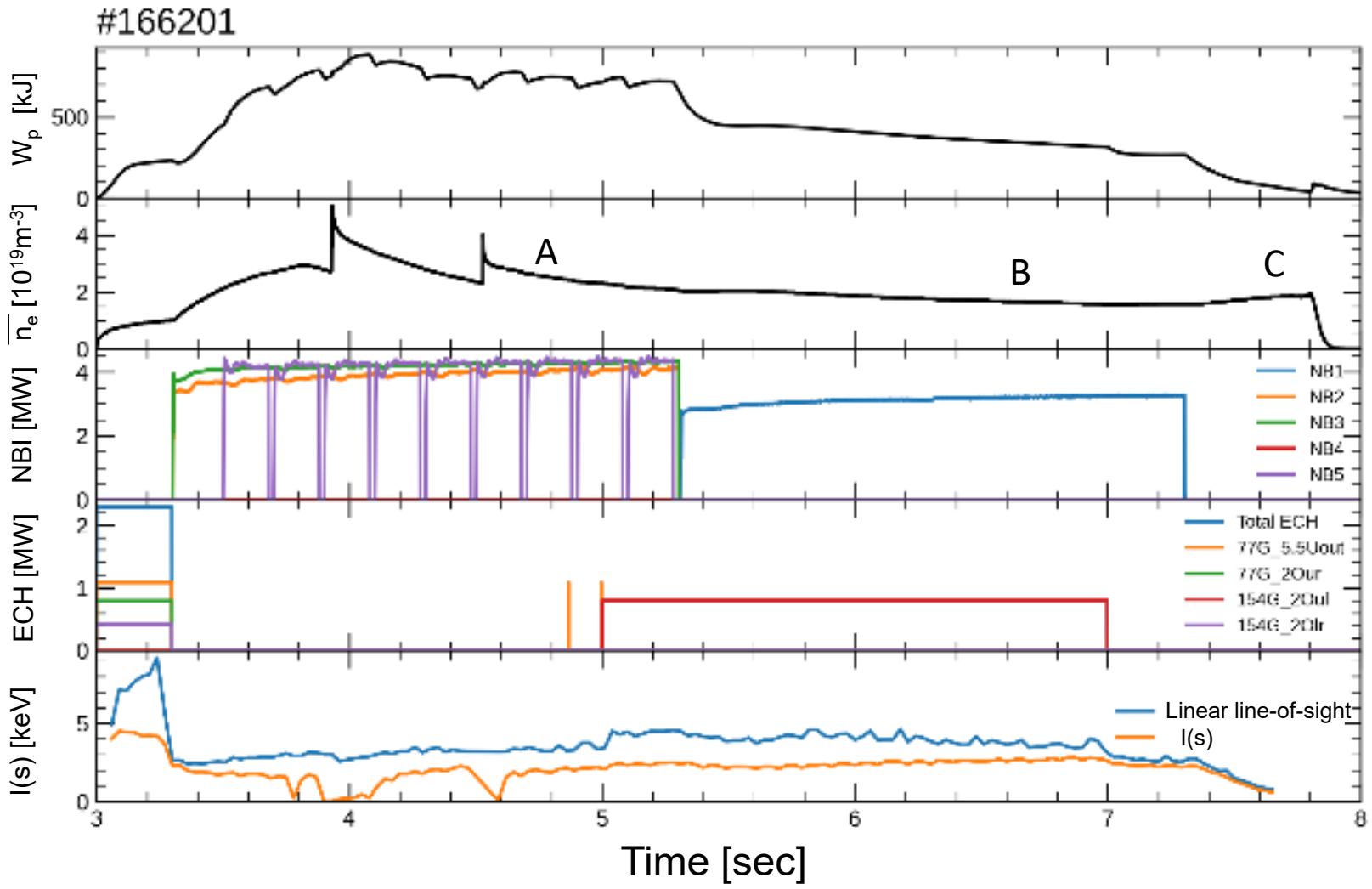
#166201
W_p [kJ]
500
0
$\overline{n_e}$ [10^{19}m^{-3}]
4
2
0
A
B
C
NBI [MW]
4
2
0
NB1
NB2
NB3
NB4
NB5
ECH [MW]
2
1
0
Total ECH
77G_5.5Uout
77G_2Our
154G_2Oul
154G_2Olr
I(s) [keV]
5
0
Linear line-of-sight
I(s)
3
4
5
6
7
8
Time [sec]

Fig.4

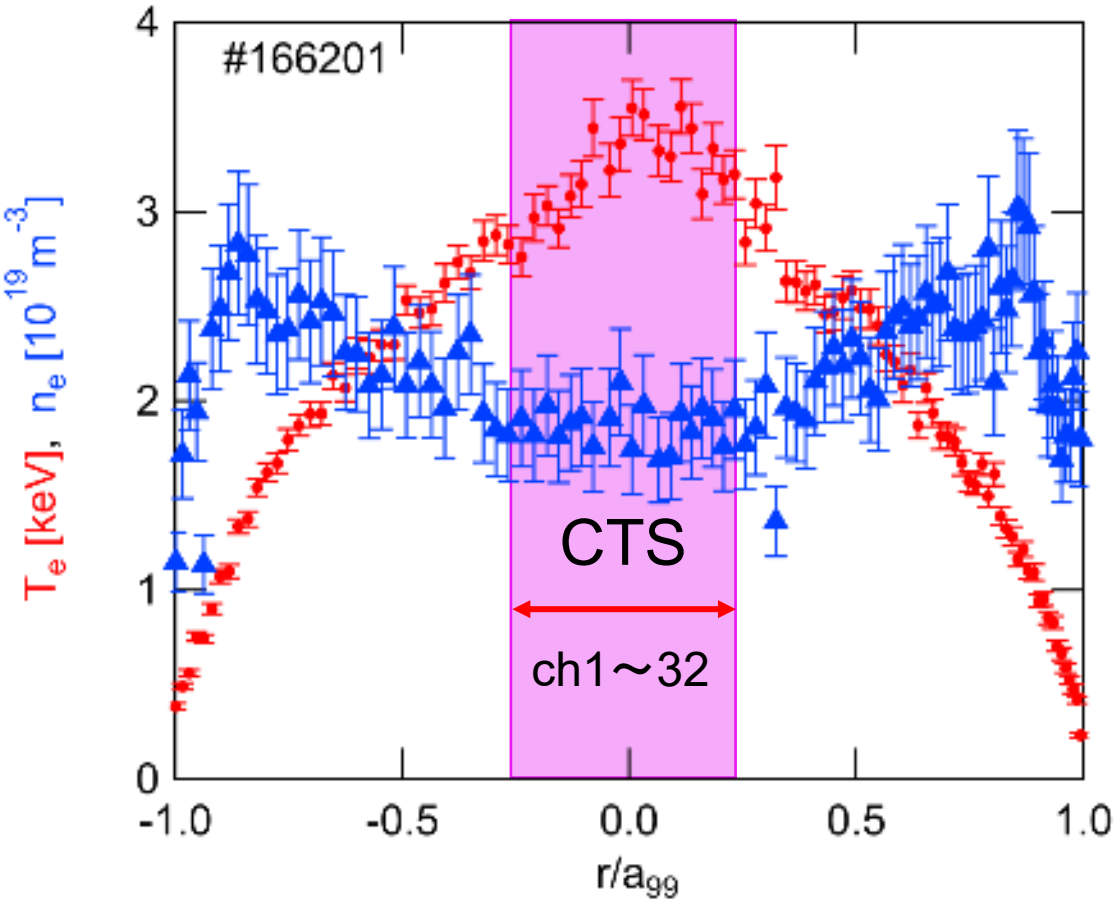

Fig.5

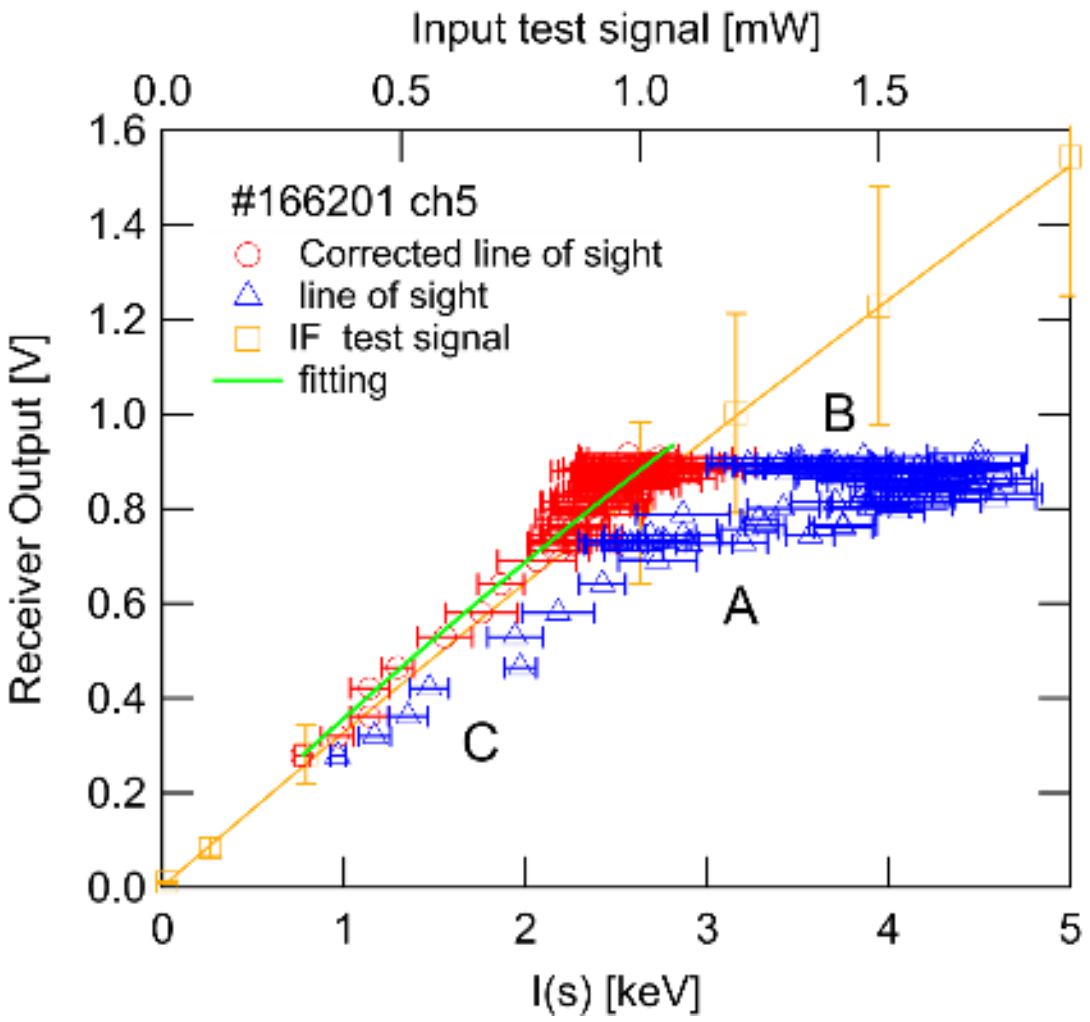
Input test signal [mW]
0.0
0.5
1.0
1.5
#166201 ch5
Corrected line of sight
line of sight
IF test signal
fitting
A
B
C
Receiver Output [V]
1.6
1.4
1.2
1.0
0.8
0.6
0.4
0.2
0.0
0
1
2
3
4
5
I(s) [keV]

Fig.6

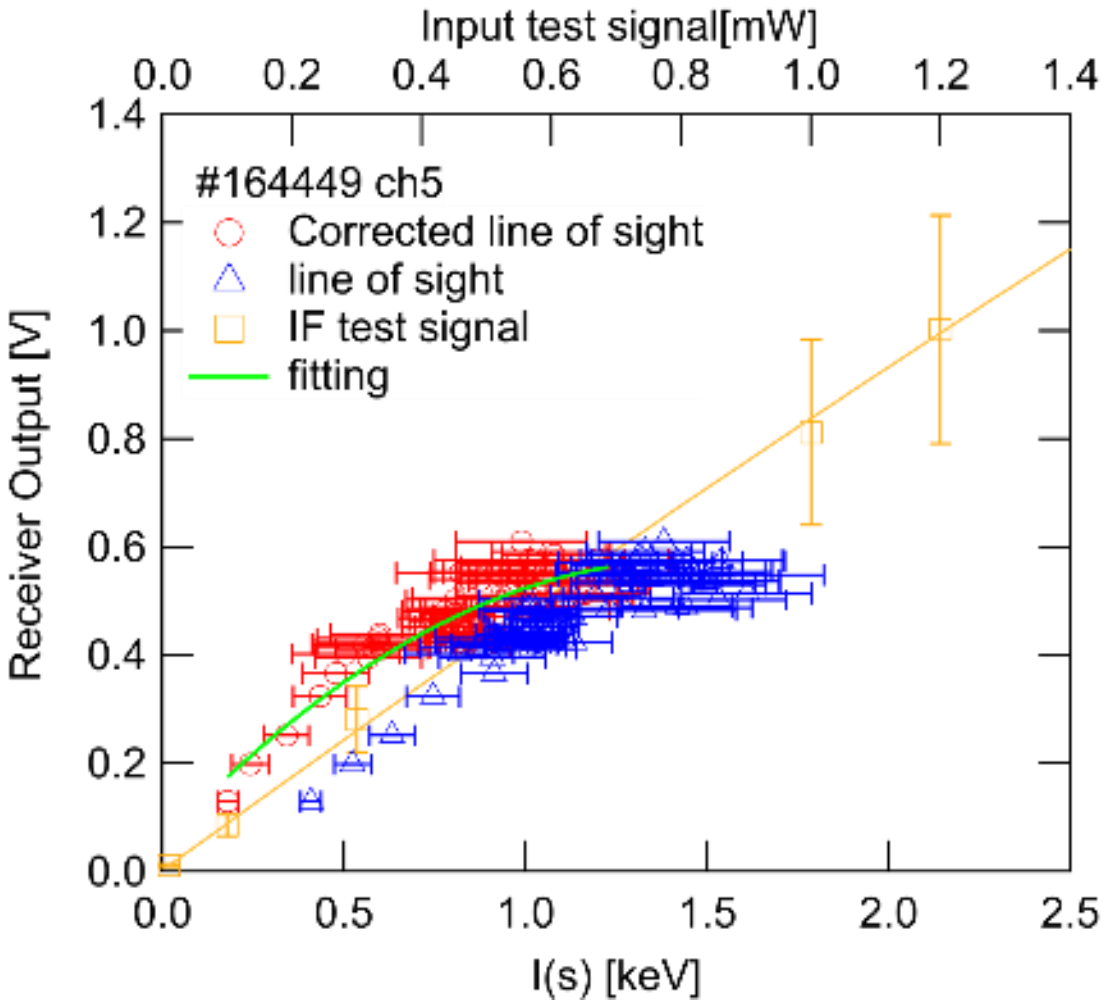
Input test signal[mW]
0.0
0.2
0.4
0.6
0.8
1.0
1.2
1.4
#164449 ch5
Corrected line of sight
line of sight
IF test signal
fitting
Receiver Output [V]
0.0
0.2
0.4
0.6
0.8
1.0
1.2
1.4
0.0
0.5
1.0
1.5
2.0
2.5
I(s) [keV]

Fig.7

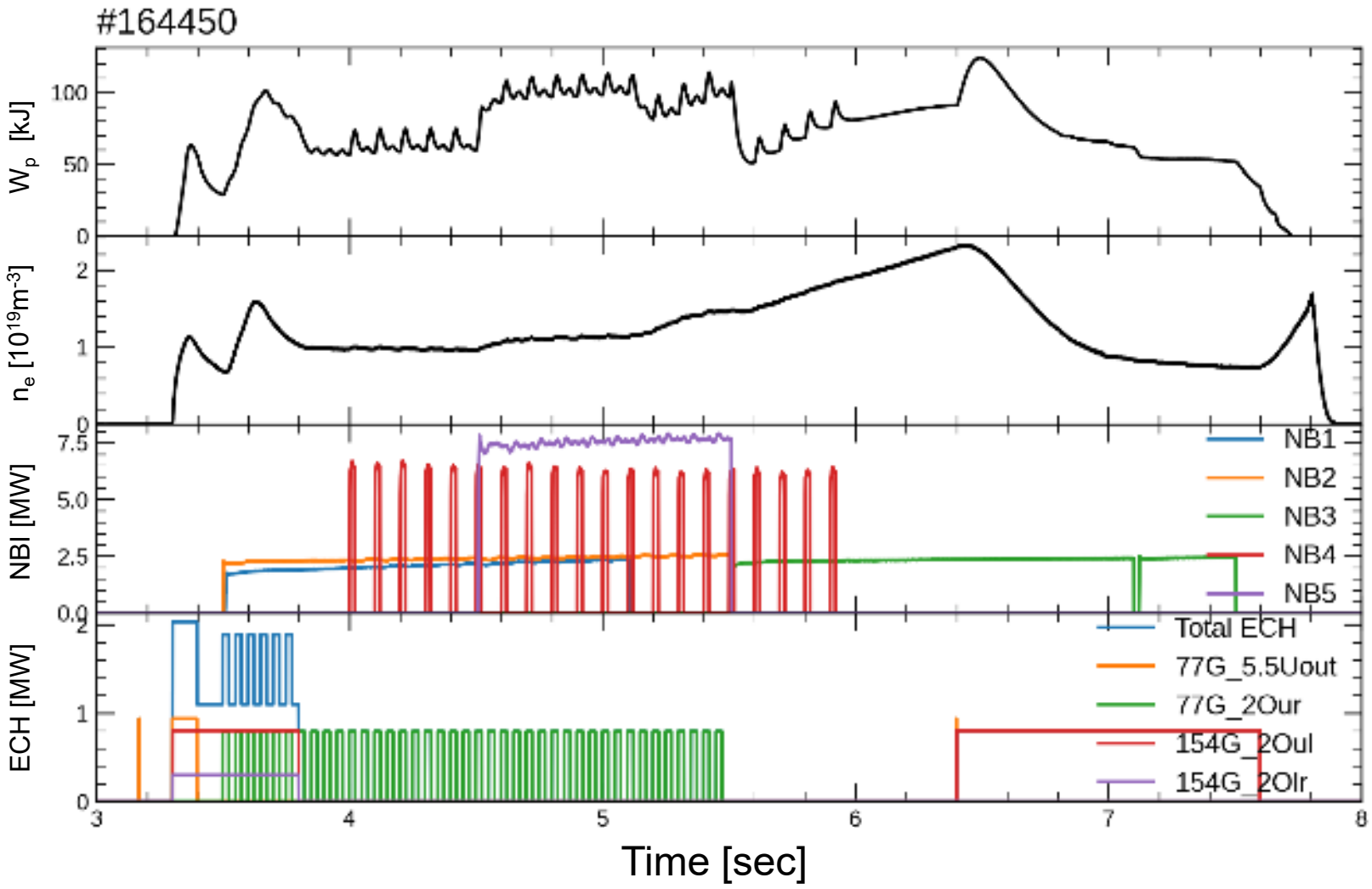
#164450
W_p [kJ]
100
50
0
n_e [$10^{19}m^{-3}$]
2
1
0
NBI [MW]
7.5
5.0
2.5
0.0
NB1
NB2
NB3
NB4
NB5
ECH [MW]
2
1
0
Total ECH
77G_5.5Uout
77G_2Our
154G_2Oul
154G_2Olr
3
4
5
6
7
8
Time [sec]

Fig.8

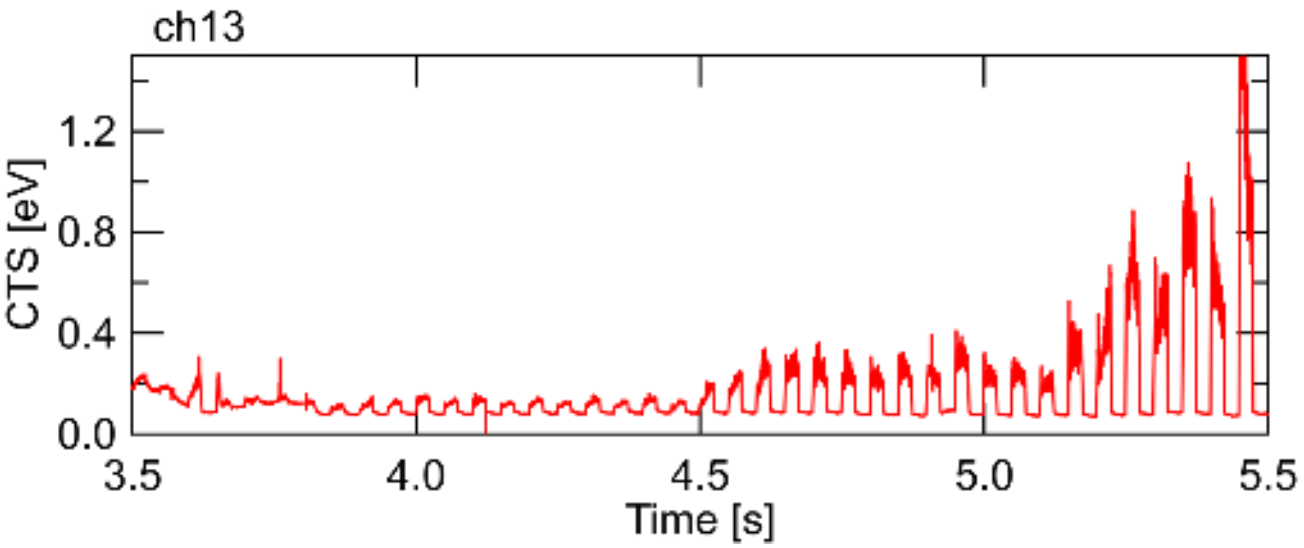

Fig.9

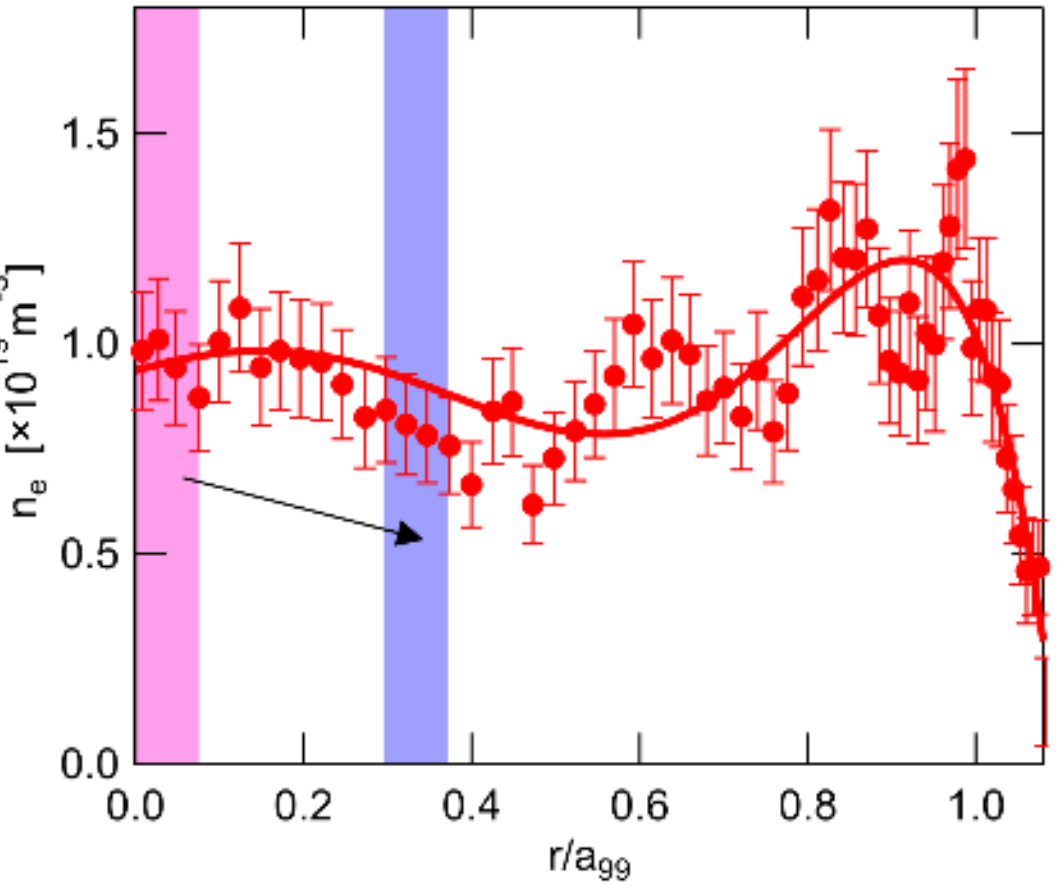

Fig.10 (a)

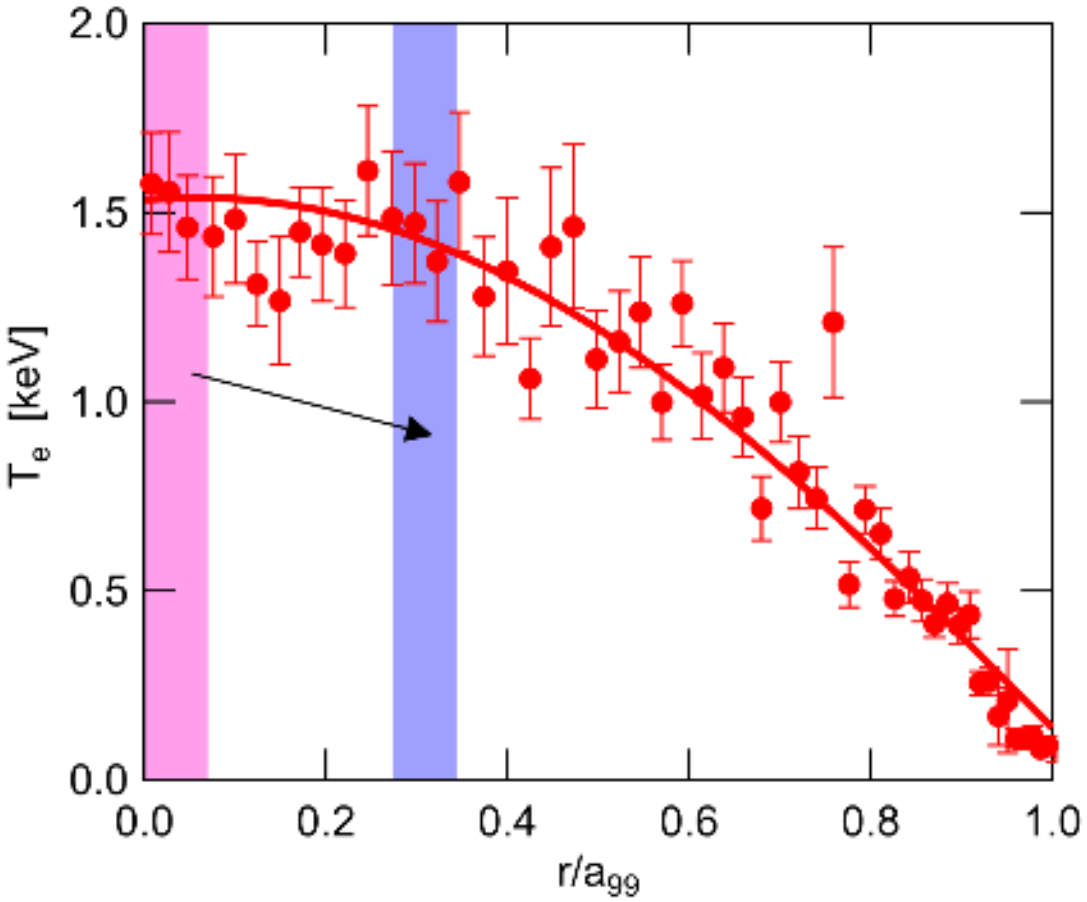

Fig.10 (b)

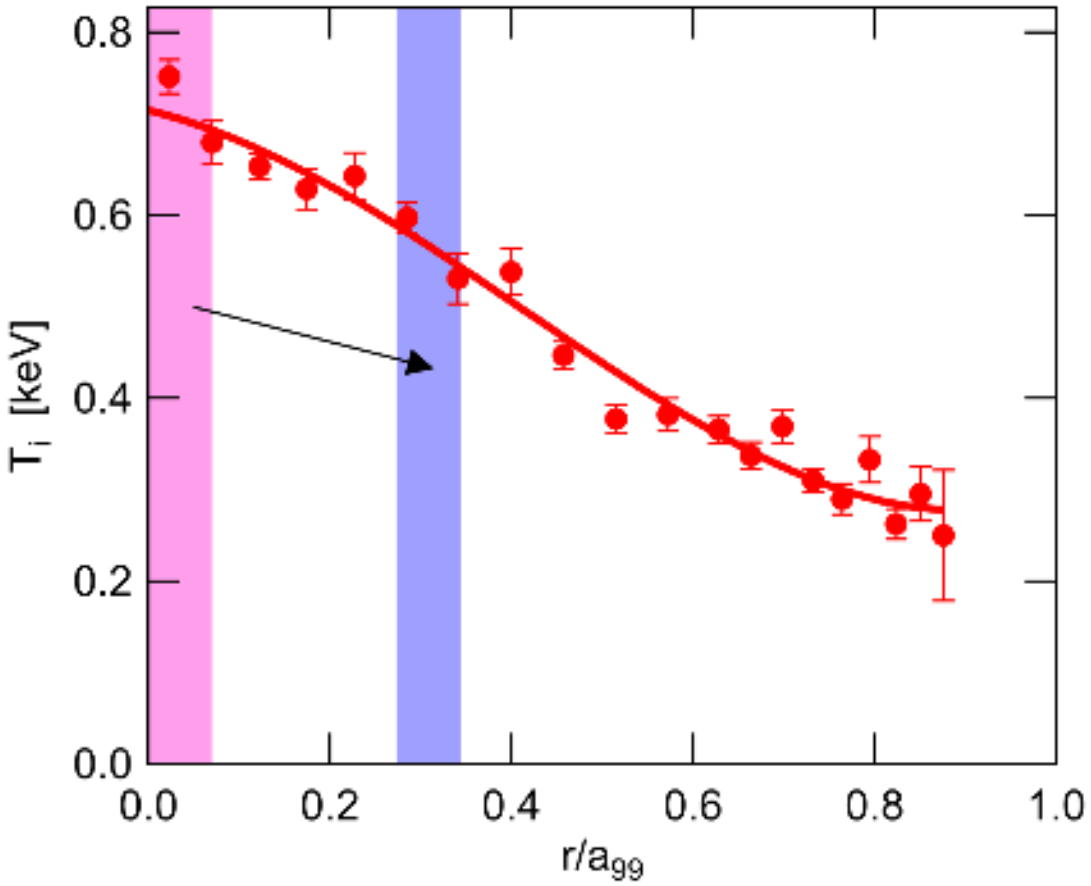

Fig.10 (c)

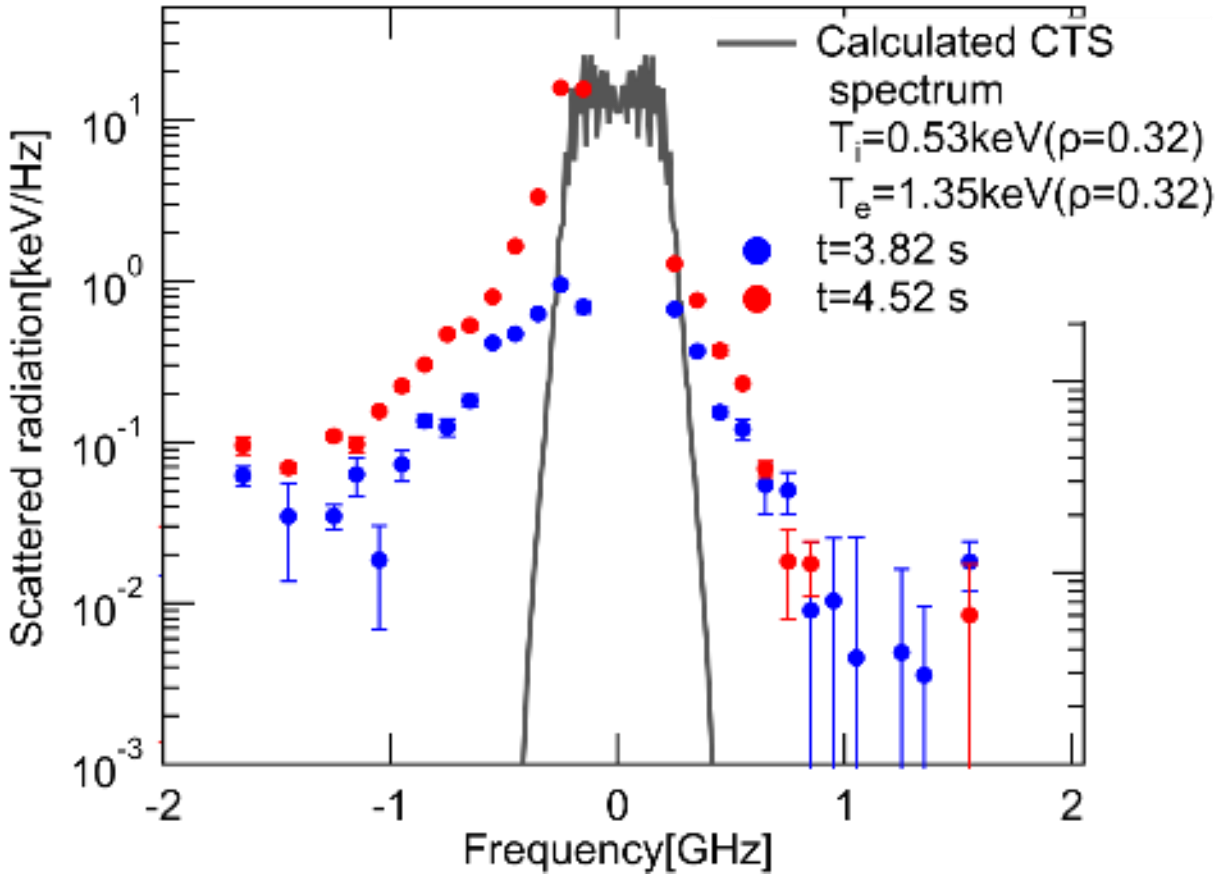
Calculated CTS
spectrum
T_i=0.53keV(ρ=0.32)
T_e=1.35keV(ρ=0.32)
t=3.82 s
t=4.52 s
Scattered radiation[keV/Hz]
10^{1}
10^{0}
10^{-1}
10^{-2}
10^{-3}
-2
-1
0
1
2
Frequency[GHz]

Fig.11